optica

Pulse-sheet chemical tomography by counterpropagating stimulated Raman scattering

Chi Yang,[1,2,†] Yali Bi,[1,2,†] Erli Cai,[1,2] Yage Chen,[1,2] Songlin Huang,[1,2] Zhihong Zhang,[1,2] and Ping Wang[1,2,*]

[1]Britton Chance Center for Biomedical Photonics, Wuhan National Laboratory for Optoelectronics-Huazhong University of Science and Technology, Wuhan, Hubei 430074, China
[2]MoE Key Laboratory for Biomedical Photonics, Collaborative Innovation Center for Biomedical Engineering, School of Engineering Sciences, Huazhong University of Science and Technology, Wuhan, Hubei 430074, China
*Corresponding author: p_wang@hust.edu.cn

Received 11 November 2020; revised 27 January 2021; accepted 3 February 2021 (Doc. ID 414723); published 12 March 2021

Large-volumetric optical tomography with molecular specificity has long been pursued to tackle the challenge of dissecting both structural and chemical organization of complicated biological tissues. Here, based on counterpropagating femtosecond pulse laser trains and stimulated Raman scattering, we report pulse-sheet chemical tomography (PCT), which allows label-free bond-selective three-dimensional imaging of large intact tissues. To prove the concept, we demonstrate vibrational tomography of highly scattering bone tissue with lateral resolution of 16.4 μm and axial resolution of 24.5 μm, over a large field of view of 8 × 8 × 1.6 mm^3 in a mouse skull with scalp. PCT resolves the trade-off between focal depth and spatial resolution, and offers unique biomedical and clinical prospects for optical tomography of tissues and organs in the future.

https://doi.org/10.1364/OPTICA.414723

1. INTRODUCTION

Optical microscopy is revolutionizing modern biology by its superior advantages in decoding of individual cells and complex tissues structurally and genetically [1,2]. However, for large-tissue tomography, only a few optical methodologies have been successful so far, including optical coherence tomography (OCT) [3], photoacoustic computed tomography (PACT) [4], light-sheet microscopy [5], and other modalities. In contrast to computed tomography (CT) [6], magnetic resonance imaging (MRI) [7] and positron-emission tomography (PET) [8], the optical tools possess priorities in molecular specificity, spatial resolution, and radiation safety, but never in tomographic depth due to strong optical scattering [9,10]. Only with bright fluorescent labeling do confocal and nonlinear microscopes allow optical sectioning in tissues by pinhole or optical nonlinear effect. Even so, the imaging depth is superficial and restricted to ∼1 mm across a very limited field of view (FOV) [11]. Park and his colleagues performed submicrometer-resolution *in vivo* imaging of a labeled mouse brain through the intact skull with an adaptive system [12]. The label-free OCT delivers low coherence light into the tissue and returns anatomical images by tissue reflection at different depths [13], but the penetration depth and specificity of the contrast are still not optimal. By taking advantage of negligible ultrasonic scattering in tissue, PACT achieved remarkable imaging depth up to 7 cm in mice *in vivo* [14]. However, the trade-off between penetration depth and spatial resolution remains a primary obstacle, limiting the spatial resolution of PACT from 100 to 600 μm. Recently, light-sheet and SRS microscopy implementing Bessel laser beams or other flattened beams has exhibited delicate tissue tomography with both submicrometer resolution and centimeter imaging depth, but is more suited to cleared or labeled tissues [15–20].

As evidenced by the fact that in PACT the light does penetrate very deep into the tissue, we believe in the success of large-tissue volumetric tomography solely based on light [14]. Here, we report conceptually a novel label-free pulse-sheet chemical tomography (termed PCT), in which the light sheet forms by ultrashort pulse laser-stimulating coherent Raman scattering (CRS) [21–23]. Specifically, the phase-locked femtosecond pump and Stokes laser pulses are introduced into the tissue in a counterpropagating mode [24–27] and a pulse-duration-determined light sheet forms in the fixed z plane of the tissue as the femtosecond pulse trains repeatedly encounter each other there. Essentially, the three-dimensional (3D) chemical anatomy of the tissue can be achieved by scanning the pulse-sheet plane across the sample by tuning the relative time delay between the pump and Stokes pulses. To prove the concept of PCT, we demonstrated bond-selective tomography of a highly scattering mouse skull with scalp at lateral and axial resolution of 16.4 μm and 24.5 μm (refractive index 1.37), respectively [28]. PCT substantially relieves the trade-off between optical focal depth and spatial resolution, and may potentially enable optical volumetric tomography comparable to x-ray CT, MRI, and PET in the future.

2. RESULTS AND DISCUSSION

A. Principle and Systematic Characterization of PCT

PCT possesses the intriguing capability of bond-selective chemical tomography, and the concept requires simply two counterpropagating femtosecond laser pulses, which form a single steady SRS imaging cross section in the sample [see Experimental Section (Supplement 1) and Visualization 1]. As a direct contrast, the typical SRS imaging microscope adopts spatially and temporally combined pump and Stokes lasers propagating in the same direction. For optical sectioning, the SRS signal only arises at the laser focus as the energy difference between the pump and Stokes photons matches the vibrational transition of specific molecules (see Experimental Section, Fig. S1, Supplement 1). Figure 1 illustrates the principle and schematic setup of the PCT system (picture of the PCT setup in Fig. S2, Supplement 1). Specifically, a ∼100 fs pump laser at ∼800 nm and a ∼200 fs Stokes laser at 1040 nm are phase-locked and synchronized at an 80 MHz repetition rate. To realize 3D tomography, the two ultrafast pulse lasers are further scanned in the $x-y$ plane by two synchronized galvanometers and focused into the sample with $f=75$ mm achromatic doublet lenses in opposite directions. As a result, the counterpropagating pump and Stokes pulse trains repeatedly encounter each other on one fixed cross-sectional plane of the sample, where the vibrational SRS signals of the target biomolecules arise. The spatial thickness (W) of the formed SRS pulse sheet, reflecting the axial imaging resolution of PCT, can be described by the formula: $W=c\times\tau/2n\sim 20$ μm, in which c represents the speed of the light, n is the refractive index of the biological tissues (n: 1.37), and τ follows the broader pulse duration of either pump or Stokes laser (see detailed calculation in Note S1, Supplement 1). Here, the axial resolution gains an additional factor of 2 due to the SRS process in counterpropagating mode (see Fig. S3, Supplement 1). It is worthwhile to note that higher spatial resolution can be achieved by applying shorter laser pulses. In addition, the SRS signal will not be produced in the rest of the cross-sectional plane of the sample, where the pulse trains always miss the temporal overlapping. To scan the pulse-sheet imaging plane in the axial direction, we simply tune the relative time delay, $2\Delta t$, between the pump and Stokes pulses. As shown in Fig. 1(a), the SRS imaging layers shift exactly as $\Delta Z_i=c\times\Delta t_i/n$. Meanwhile, two synchronized two-axis galvanometers are equipped for each laser beam to provide fast and accurate point-to-point lateral scanning in the $x-y$ plane [Fig. 1(b) and Fig. S4(a), Supplement 1]. The lateral resolution of PCT is determined by the focal length of the lens and the size of the incident laser beams (Note S1, Supplement 1). A large area photodiode with resonant amplifier is installed as close as possible to the sample to collect the highly scattered pump photons for lock-in detection of SRS signals.

To experimentally validate the performance of the PCT system, we conducted 3D SRS imaging of a droplet of glyceryl trioleate (TO) sealed between two coverslips, 10 μm polystyrene (PS) beads, and an intact polymethyl methacrylate (PMMA) microneedle (MN) patch immerged in deuteroxide (D_2O). In Fig. S4(b), Supplement 1, the TO droplet rich in carbon–hydrogen stretching (C–H, 2800−3100 cm^{-1}) was chemically imaged in 3D by PCT with a signal-to-noise ratio (SNR) and signal-to-background ratio (SBR) measured to be 226 and 71, respectively (Fig. S4(c), (d), Supplement 1). To determine the focal depth produced by the two 75 mm lenses, we obtained a serial of SRS images of a thin TO droplet translated along the z direction (Fig. S4(e), Supplement 1). The focal depth for PCT is measured to be about 2.7 mm in full width at half-maximum (FWHM), which is very consistent with the theoretical calculation [Fig. S4(f), Note S2, Supplement 1]. The focal depth indicates how far the pulse sheet can be scanned in the z direction (ΔZ) by time delay while maintaining the SRS efficiency. But, it does not limit the size of the sample that can be imaged. In addition, for large-tissue tomography, where an imaging lens with longer focal length and smaller numerical aperture (NA) is applied, the PCT is superior to typical SRS or other

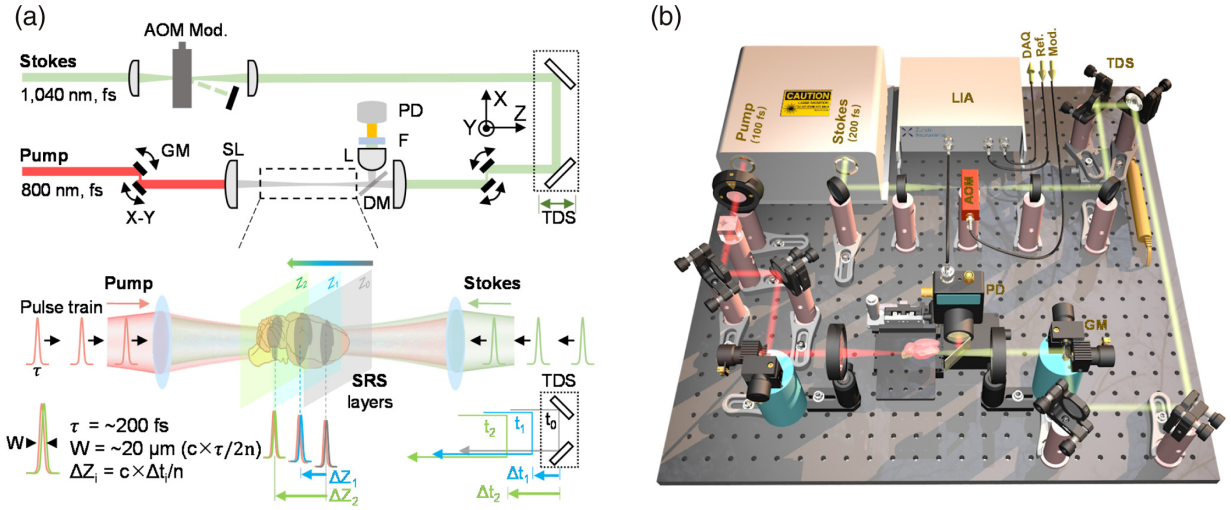

Fig. 1. Schematic of PCT. (a) Principle of PCT system. The femtosecond Stokes laser pulses coincide with the pump laser pulses in counterpropagating mode (incident beam diameter, $\Phi=2$ mm; focus length, 75 mm lens; NA = 0.013), which forms a stationary pulse-sheet plane near the laser focus for SRS tomography. The thickness (W) of the pulse sheet forming the SRS imaging layer is only determined by the pulse width τ (e.g., $W=\sim$ 20 μm as $\tau=\sim$ 200 fs). Crucially, the pulse-sheet imaging plane can be scanned in the z direction by tuning the relative time delay between the pump and Stokes pulses (TDS). An AOM is implemented to modulate the Stokes laser for further lock-in detection of SRS signal. Two synchronized two-axis GMs are applied to form the $x-y$ imaging plane. (b) Experimental schematic of the PCT setup. AOM, acousto-optic modulator; TDS, time delay scanning; GM, galvanometer; SL, scanning lens; LIA, lock-in amplifier; Ref., reference frequency from function generator; Mod., modulated radio-frequency input to AOM; DAQ, data acquisition; DM, dichroic mirror; PD, photodiode; F, filter; L, lens.

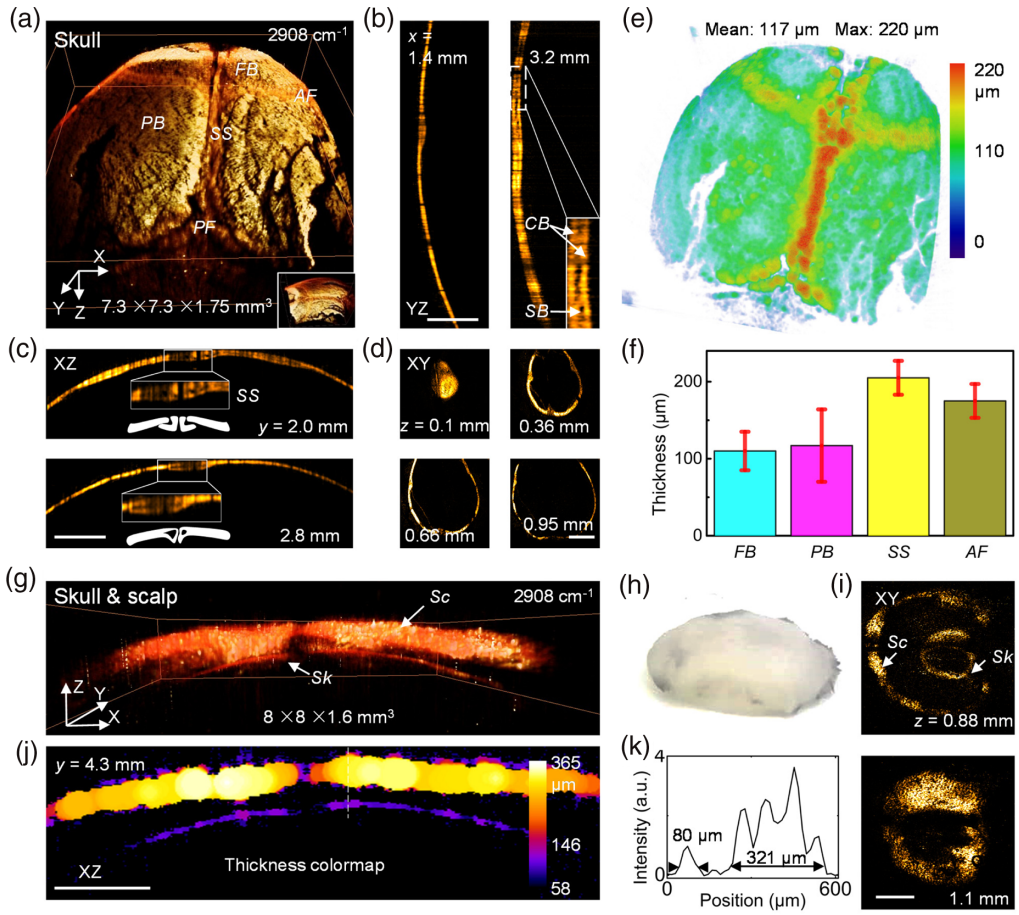

Fig. 2. PCT imaging of mouse skull and scalp. (a) 3D SRS reconstruction of mouse skull by detecting C–H stretching at 2908 cm^{-1}. FB, frontal bone; AF, anterior fontanelle; PB, parietal bone; SS, sagittal suture; PF, posterior fontanelle; (b) side; (c) front; and (d) top view images at different depths. CB, compact bone; SB, spongy bone. Inset in (c), reference models; Scale bars, (b)–(c), 1 mm; (d) 2 mm; (e) thickness color map of the skull; (f) thickness histogram at different regions. The error bars represent the standard deviation of the thickness. (g) Reconstructed 3D SRS image of mouse skull (Sk) with homologous thick scalp (Sc) at 2908 cm^{-1}; (h) photograph of the real skull with scalp; (i) cross-sectional images of Sk with Sc at $z = 0.88$ and 1.1 mm; scale bar, 2 mm; (j) thickness color map at $y = 4.3$ mm. Scale bar, 1 mm; (k) intensity profile along dashed line in (j).

nonlinear optical imaging and maintains good axial resolution solely determined by the pulse width. For traditional imaging methods, the axial resolution at the focus of 75 mm lens (e.g., Φ, 2 mm; NA, 0.013) degrades to 4.2 mm (FWHM). Meanwhile, the axial imaging resolution can be maintained in ∼24.5 μm for PCT, attributed to the SRS pulse sheet [Fig. S4(g), Supplement 1].

To characterize the spatial resolution of PCT, the PS beads in Fig. S5(a), Supplement 1, were chemically identified and imaged by detecting the SRS spectrum of C–H stretching [Fig. S5(b), Supplement 1]. The FWHM of the 10 μm PS beads was measured to be 17.9 and 22.7 μm in lateral and axial directions, respectively. The results are consistent with our theoretical predictions of the spatial resolution of PCT (see Note S1, Supplement 1). In Figs. S5(c)–(g), Supplement 1, we further performed label-free 3D chemical tomography of a D_2O immersed MN patch ($6.5 \times 6.5 \times 1.0\ mm^3$), which is hard to image by OCT and PACT without labeling [29]. Here, PCT allows high-resolution and bond-selective volumetric tomography for both the MN patch (2908 cm^{-1}, Fig. S5(g), Supplement 1) and surrounding D_2O (2446 cm^{-1}). Especially, the individual PMMA needles with diameter of 300 μm and height of 600 μm on the patch can be visualized in great detail (Fig. S5(e), Supplement 1). The spectral resolution of PCT was characterized by dimethyl sulfoxide (DMSO) to be 160 cm^{-1} (Fig. S5(h), Supplement 1), which is limited by the trade-off between spectral width and pulse width of the femtosecond lasers.

B. Large-Scale Volumetric Tomography of Highly Scattering Bone Tissue

The mouse skull with thick scalp is highly heterogeneous and scattering for photons, which results in a challenge for high-resolution optical tomography. Figure 2(a) presents the 3D morphological structure of a piece of fresh mouse skull, which is depicted by PCT at a Raman shift of 2908 cm^{-1}, indicating a large amount of collagen in bone (Visualization 2). The distinct features of frontal bone (FB), anterior fontanelle (AF), parietal bone (PB), sagittal suture (SS), and posterior fontanelle (PF) were revealed in different regions of the intact skull ($7.3 \times 7.3 \times 1.75\ mm^3$ in size). Even the cracks and intercavities, where the collagen is absent, can be clearly observed in real details in the skull. Especially from the sagittal and coronal images, we are able to distinguish the double-layer structure of compact bones (CBs), possible spongy bones (SBs) in between [Fig. 2(b)] [30] and the fine calvarial fusion structures [Fig. 2(c)] in the SS region [31], owing to the strong photon scattering and attenuation (Fig. S6, Supplement 1), which

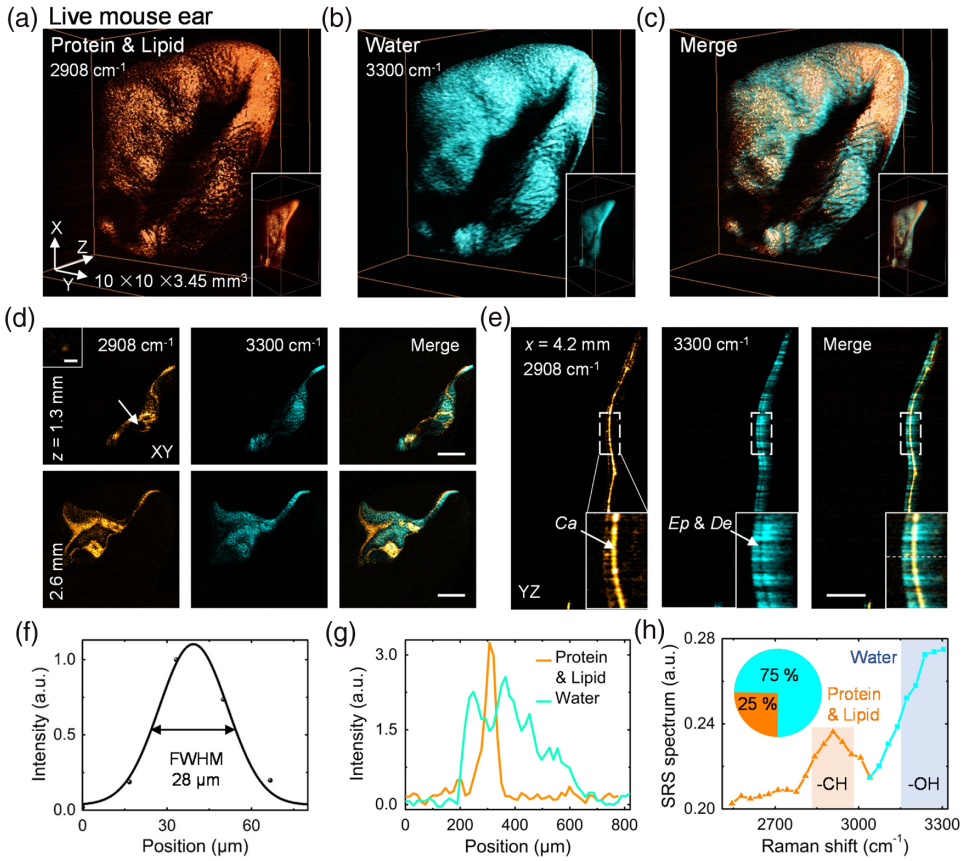

Fig. 3. Noninvasive PCT imaging of mouse ear *in vivo*. (a)–(b) 3D view of protein and lipid [(a), 2908 cm^{-1}) and water (b), 3300 cm^{-1}] in mouse ear; inset: side view; (c) color overlay image of (a)–(b). (d) cross-sectional images of protein and lipid and water at different tissue depths; scale bars, 2 mm; inset: zoom-in image of a protein/lipid granule indicated by the white arrow; scale bar, 100 μm; (e) side view at depth of $x = 4.2$ mm. Ca, cartilage; Ep, epidermis; De, dermis; scale bars, 1 mm. (f) cross-sectional profile of the selected protein/lipid granule in (d); (g) intensity profiles along dashed line in (e), illustrating the distribution of the bilayer structure of the mouse ear; (h) SRS spectra indicating that the content ratio of protein and lipid (C–H, 2908 cm^{-1}) to water (O–H, 3300 cm^{-1}) in mouse ear is ∼1 : 3.

are difficult to image by other tomographic methods. Figure 2(d) shows the skeleton maps of the skull at different depths along the z axis, and the profiles of the shell illustrate apparent inhomogeneity of skull in thickness. By the overall thickness analysis, the region with maximum protein thickness in the whole skull is found to be SS, where the average thickness is about ∼220 μm [Fig. 2(e)]. Comparatively, the rest of the area of the skull, particularly PB, exhibits significant heterogeneity, with an average thickness of about 110 μm [Fig. 2(f)]. We further performed 3D PCT imaging of a large piece of mouse skull with homologous thick scalp on the top. Figure 2(g) presents the spatial distributions of the skull and scalp, which were flattened to a size about 8 × 8 × 1.6 mm^3. In contrast to the photograph of the tissue [Fig. 2(h)], Fig. 2(i) gives the cross-sectional map of both skull and scalp along the $x - y$ plane at z depths of 0.88 and 1.0 mm, respectively. The color map in Fig. 2(j) shows the thickness distribution of the whole tissue, and the SRS intensity profile [Fig. 2(k)] along the dashed line in Fig. 2(j) measured the thickness of the skull and scalp to be 80 and 321 μm, respectively. All these imaging results confirm that PCT is capable of chemical tomography and 3D morphological reconstruction of large and highly scattering bone tissues. In Table S1, Supplement 1, we compare the performance of PCT with other tissue tomography methods.

C. Chemical Tomography of Live Mouse Ear

By providing the vital noninvasive imaging, PCT possesses the unique advantage of bond-selective chemical tomography *in vivo* over many other imaging methods. In Figs. 3(a)–3(c), we demonstrated chemical imaging of protein and lipid (C–H, 2908 cm^{-1}) and water (O–H, 3300 cm^{-1}) distribution inside a live mouse ear (Visualization 3). The size of the whole mouse ear is about 10.0 × 10.0 × 3.45 mm^3, which structurally consists of epithelial, dermis, cartilage layers, and numerous hair follicles, etc. [32]. Figure 3(d) illustrates the spatial distributions of cartilage and water in ear at a z depth of 1.3 and 2.6 mm, respectively. In the cross section along the $y - z$ plane [Fig. 3(e)], we observed the double layers of water and a single cartilage layer containing lipid and protein in the middle of the live mouse ear. This implies that the surface of mouse ear is full of intercellular fluid [33,34]. Figure 3(g) shows the cross-sectional profiles of protein/lipid and water distributed in the mouse ear [along the indicated line in Fig. 3(e)], and the thickness of cartilage and double-layer water is about 182 and 438 μm, respectively. We also characterized one protein/lipid granule in the ear; the size was measured to be ∼28 μm in FWHM [$x - y$, Fig. 3(f)] [35]. In Fig. 3(h), we acquired the SRS spectra by tuning the wavelength of pump laser when imaging the mouse pinna, and the Raman bands of both C–H and O–H can be clearly identified. The volumetric ratio of protein and lipid to water in the

mouse ear was measured to be about 1:3 (data processing in Note S3, Supplement 1), suggesting that the biological systems consist mainly of water [36,37].

3. CONCLUSION

We present what we believe is a new concept of noninvasive optical tomography with chemical specificity and demonstrate large-scale tomography of highly scattering bone tissue with superiority in many aspects. The centimeter-sized mouse skull with scalp *ex vivo* and mouse ear *in vivo* were chemically 3D-mapped without clearing. The concept of PCT proves the major advantage in label-free SRS tomography of large tissues, where PCT meets the needs of a large FOV and long working distance in centimeters. For potential clinical applications, PCT is well suited for pathological diagnosis of cancerous tissues without labeling and frozen section.

Due to the thin imaging sheet formed by the counterpropagating pump and Stokes pulses, PCT has about 2 orders of magnitude of degradation in the SRS signal, in contrast to the traditional copropagating SRS. To reach a similar axial resolution ($\sim$25 μm) in copropagating SRS, the required NA of the objective is calculated to be $\sim$0.2. The commercial objectives, such as Carl Zeiss Epiplan-Apochromat 5 × NA 0.2 and Nikon CFI Plan Apo Lambda 4 × NA 0.2, are available. Although the lateral resolution will improve, both the FOV and the working distance will be strictly limited in the range of $\sim 5-10$ mm. So far, the penetration depth of PCT in tissue may not surpass many current imaging modalities because of SRS signals that are too weak from intrinsic biomolecules for detection. However, PCT is a new concept for large-tissue tomography, which converts the fast traveling laser pulse at a speed of c to a stationary pulse sheet for tomography. The significance of the concept will also be reflected in many aspects.

Since the tissue has less temporal dispersion, the axial resolution of PCT can be further improved to <2 μm by applying 10 fs or attosecond pulse laser over a large FOV, but at the expense of spectral resolution. Moreover, the NIR-II or IR lasers with longer wavelength and less scattering in tissue can ensure significant extension of the penetration depth of PCT without degradation of axial resolution. In particular, this methodology also applies to fluorescence multiphoton imaging, photoacoustic imaging, and other imaging modalities, as long as the labeled reports or tags require excitation from two pulses in different wavelengths or polarizations. Thus, with the aid of strong fluorescence labeling, we believe the signal intensity and imaging depth in tissue could be substantially improved. The pulse-sheet-based 3D volumetric tomography with improved performances in multiple directions is expected to contribute a variety of research frontiers and potentially become a versatile optical alternative for organ or body tomography in routine clinical applications in the future.

Funding. National Key Research and Development Program of China (2016YFA0201403); National Natural Science Foundation of China (62075076, 61675075, 81827901, 61721092); Science Fund for Creative Research Groups of China (61421064); Innovation Fund of the Wuhan National Laboratory for Optoelectronics.

Acknowledgment. C. Y. and Y. L. B. carried out the construction of the PCT system and performed experiments. C. Y. and Y. L. B. prepared the biological samples. C. Y., Y. L. B., and P. W. analyzed the data and wrote the paper with input from all authors. P. W., C. Y., and Y. L. B. conceived the concept. P. W. supervised the experiments and the project.

Disclosures. PW, CY, YB: Huazhong University of Science and Technology, ZL 2019 1 1001116.6 (P).

Supplemental document. See Supplement 1 for supporting content.

[†]These authors contributed equally to this work.

REFERENCES

1. S. G. Megason and S. E. Fraser, "Imaging in systems biology," Cell **130**, 784–795 (2007).
2. R. Weissleder and M. J. Pittet, "Imaging in the era of molecular oncology," Nature **452**, 580–589 (2008).
3. E. M. Frohman, J. G. Fujimoto, T. C. Frohman, P. A. Calabresi, G. Cutter, and L. J. Balcer, "Optical coherence tomography: a window into the mechanisms of multiple sclerosis," Nat. Clin. Pract. Neurol. **4**, 664–675 (2008).
4. L. V. Wang and S. Hu, "Photoacoustic tomography: in vivo imaging from organelles to organs," Science **335**, 1458–1462 (2012).
5. F. F. Voigt, D. Kirschenbaum, E. Platonova, S. Pages, R. A. A. Campbell, R. Kastli, M. Schaettin, L. Egolf, A. van der Bourg, P. Bethge, K. Haenraets, N. Frezel, T. Topilko, P. Perin, D. Hillier, S. Hildebrand, A. Schueth, A. Roebroeck, B. Roska, E. T. Stoeckli, R. Pizzala, N. Renier, H. U. Zeilhofer, T. Karayannis, U. Ziegler, L. Batti, A. Holtmaat, C. Luscher, A. Aguzzi, and F. Helmchen, "The mesoSPIM initiative: open-source light-sheet microscopes for imaging cleared tissue," Nat. Methods **16**, 1105–1108 (2019).
6. S. R. Cherry, "Multimodality imaging: beyond PET/CT and SPECT/CT," Semin. Nucl. Med. **39**, 348–353 (2009).
7. M. S. Judenhofer, H. F. Wehrl, D. F. Newport, C. Catana, S. B. Siegel, M. Becker, A. Thielscher, M. Kneilling, M. P. Lichy, M. Eichner, K. Klingel, G. Reischl, S. Widmaier, M. Rocken, R. E. Nutt, H. J. Machulla, K. Uludag, S. R. Cherry, C. D. Claussen, and B. J. Pichler, "Simultaneous PET-MRI: a new approach for functional and morphological imaging," Nat. Med. **14**, 459–465 (2008).
8. M. Levine and J. Julian, "Imaging: PET-CT imaging in non-small-cell lung cancer," Nat. Rev. Clin. Oncol. **6**, 619–620 (2009).
9. V. Ntziachristos, "Going deeper than microscopy: the optical imaging frontier in biology," Nat. Methods **7**, 603–614 (2010).
10. S. Yoon, M. Kim, M. Jang, Y. Choi, W. Choi, S. Kang, and W. Choi, "Deep optical imaging within complex scattering media," Nat. Rev. Phys. **2**, 141–158 (2020).
11. W. R. Zipfel, R. M. Williams, and W. W. Webb, "Nonlinear magic: multiphoton microscopy in the biosciences," Nat. Biotechnol. **21**, 1369–1377 (2003).
12. J. H. Park, W. Sun, and M. Cui, "High-resolution in vivo imaging of mouse brain through the intact skull," Proc. Natl. Acad. Sci. USA **112**, 9236–9241 (2015).
13. S. H. Yun and S. J. J. Kwok, "Light in diagnosis, therapy and surgery," Nat. Biomed. Eng. **1**, 0008 (2017).
14. L. V. Wang and J. Yao, "A practical guide to photoacoustic tomography in the life sciences," Nat. Methods **13**, 627–638 (2016).
15. R. M. Power and J. Huisken, "A guide to light-sheet fluorescence microscopy for multiscale imaging," Nat. Methods **14**, 360–373 (2017).
16. T. A. Planchon, L. Gao, D. E. Milkie, M. W. Davidson, J. A. Galbraith, C. G. Galbraith, and E. Betzig, "Rapid three-dimensional isotropic imaging of living cells using Bessel beam plane illumination," Nat. Methods **8**, 417–423 (2011).
17. P. Mahou, J. Vermot, E. Beaurepaire, and W. Supatto, "Multicolor two-photon light-sheet microscopy," Nat. Methods **11**, 600–601 (2014).
18. X. Chen, C. Zhang, P. Lin, K.-C. Huang, J. Liang, J. Tian, and J.-X. Cheng, "Volumetric chemical imaging by stimulated Raman projection microscopy and tomography," Nat. Commun. **8**, 15117 (2017).
19. M. Wei, L. Shi, Y. Shen, Z. Zhao, A. Guzman, L. J. Kaufman, L. Wei, and W. Min, "Volumetric chemical imaging by clearing-enhanced stimulated Raman scattering microscopy," Proc. Natl. Acad. Sci. USA **116**, 6608–6617 (2019).
20. A. H. Hill, B. Manifold, and D. Fu, "Tissue imaging depth limit of stimulated Raman scattering microscopy," Biomed. Opt. Express **11**, 762–774 (2020).
21. C. W. Freudiger, W. Min, B. G. Saar, S. Lu, G. R. Holtom, C. He, J. C. Tsai, J. X. Kang, and X. S. Xie, "Label-free biomedical imaging with high sensitivity by stimulated Raman scattering microscopy," Science **322**, 1857–1861 (2008).
22. C. H. Camp, Jr. and M. T. Cicerone, "Chemically sensitive bioimaging with coherent Raman scattering," Nat. Photonics **9**, 295–305 (2015).

23. A.-G. Alba, M. Richa, L. E. Seong, and O. P. Eric, "Biological imaging with coherent Raman scattering microscopy: a tutorial," J. Biomed. Opt. **19**, 071407 (2014).
24. J. X. Cheng, A. Volkmer, and X. S. Xie, "Theoretical and experimental characterization of coherent anti-Stokes Raman scattering microscopy," J. Opt. Soc. Am. B **19**, 1363–1375 (2002).
25. A. Compaan and S. Chandra, "Coherent anti-Stokes Raman scattering with counterpropagating laser beams," Opt. Lett. **4**, 170–172 (1979).
26. D. J. Rakestraw, R. L. Farrow, and T. Dreier, "Two-dimensional imaging of OH in flames by degenerate four-wave mixing," Opt. Lett. **15**, 709–711 (1990).
27. C. J. Kliewer, "High-spatial-resolution one-dimensional rotational coherent anti-Stokes Raman spectroscopy imaging using counterpropagating beams," Opt. Lett. **37**, 229–231 (2012).
28. I. M. Berke, J. P. Miola, M. A. David, M. K. Smith, and C. Price, "Seeing through musculoskeletal tissues: improving in situ imaging of bone and the lacunar canalicular system through optical clearing," Plos One **11**, e0150268 (2016).
29. R. Z. Seeni, X. Yu, H. Chang, P. Chen, L. Liu, and C. Xu, "Iron oxide nanoparticle-powered micro-optical coherence tomography for in situ imaging the penetration and swelling of polymeric microneedles in the skin," ACS. Appl. Mater. Interfaces **9**, 20340–20347 (2017).
30. Y.-J. Zhao, T.-T. Yu, C. Zhang, Z. Li, Q.-M. Luo, T.-H. Xu, and D. Zhu, "Skull optical clearing window for in vivo imaging of the mouse cortex at synaptic resolution," Light Sci. Appl. **7**, 17153 (2018).
31. C. R. Chung, K. Tsuji, A. Nifuji, T. Komori, K. Soma, and M. Noda, "Micro-CT evaluation of tooth, calvaria and mechanical stress-induced tooth movement in adult Runx2/Cbfa1 heterozygous knock-out mice," J. Med. Dent. Sci. **51**, 105–113 (2004).
32. O. Liba, M. D. Lew, E. D. SoRelle, R. Dutta, D. Sen, D. M. Moshfeghi, S. Chu, and A. de la Zerda, "Speckle-modulating optical coherence tomography in living mice and humans," Nat. Commun. **8**, 15845 (2017).
33. M. Egawa, T. Hirao, and M. Takahashi, "In vivo estimation of stratum corneum thickness from water concentration profiles obtained with Raman spectroscopy," Acta Derm. Venereol **87**, 4–8 (2007).
34. C. Eklouh-Molinier, V. Gaydou, E. Froigneux, P. Barlier, V. Couturaud, M. Manfait, and O. Piot, "In vivo confocal Raman microspectroscopy of the human skin: highlighting of spectral markers associated to aging via a research of correlation between Raman and biometric mechanical measurements," Anal. Bioanal. Chem. **407**, 8363–8372 (2015).
35. C. L. Evans, E. O. Potma, M. Puoris'haag, D. Cote, C. P. Lin, and X. S. Xie, "Chemical imaging of tissue in vivo with video-rate coherent anti-Stokes Raman scattering microscopy," Proc. Natl. Acad. Sci. USA **102**, 16807–16812 (2005).
36. M. Marco, M. Giovanna, C. Silvana, S. Silvia, F. Francesca, L. Caterina, and P. Giovanni, "Does skin hydration influence keratinocyte biology? In vivo evaluation of microscopic skin changes induced by moisturizers by means of reflectance confocal microscopy," Skin Res. Technol. **19**, 299–307 (2013).
37. S. Bielfeldt, V. Schoder, U. Ely, A. Van Der Pol, J. De Sterke, and K.-P. Wilhelm, "Assessment of human stratum corneum thickness and its barrier properties by in-vivo confocal Raman spectroscopy," Int. J. Cosmetic Sci. **31**, 479–480 (2009).